Journal of Computational Physics 229 (2010) 7030–7041

Contents lists available at ScienceDirect

Journal of Computational Physics

journal homepage: www.elsevier.com/locate/jcp

# Adaptive variational multiscale methods for incompressible flow based on two local Gauss integrations ☆

Haibiao Zheng *, Yanren Hou, Feng Shi

*College of Science, Xi'an Jiaotong University, Xi'an 710049, China*

ARTICLE INFO

*Article history:*
Received 23 September 2009
Received in revised form 19 May 2010
Accepted 25 May 2010
Available online 2 June 2010

*Keywords:*
Navier–Stokes equations
Variational multiscale methods
*h*-Adaptive
Two local Gauss integrations

ABSTRACT

We consider variational multiscale (VMS) methods with *h*-adaptive technique for the stationary incompressible Navier–Stokes equations. The natural combination of VMS with adaptive strategy retains the best features of both methods and overcomes many of their deficits. A reliable a posteriori projection error estimator is derived, which can be computed by two local Gauss integrations at the element level. Finally, some numerical tests are presented to illustrate the method's efficiency.



## 1. Introduction

In the numerical simulation of incompressible flows, there are still many challenges, such as, how to control the accuracy of a numerical approximation for the solutions, which may be degraded by the local singularities or the singularity in the computational domain. Since the work by Babuska and Rheinboldt [1,2], adaptive control based on a posteriori error estimates has become very attractive. Many researchers pay their attention on the field of a posteriori error estimators and have got lots of good results in the last few decades, for example, [3–5] derive the residual-based a posteriori error estimate. Deriving a posteriori error estimates for the Stokes equations also has received much attention (see [4,6–8] and so on), for the Navier–Stokes equation, see [9]. Many people also develop some other methods, like, the estimators based on the element residual, based on evaluating integrals of the residuals or associated with spatial averages. Besides, the recovery type error estimators are discussed in [10–16], recently.

Variational multiscale methods are designed to deal with incompressible flow, which define the large scales in a different way, namely by projection into appropriate subspaces, see Guermond [17], Hughes et al. [18–20] and Layton [21], and other literatures on VMS methods [21–26]. The idea of two local Gauss integrations has been considered to deal with the variational multiscale methods (such as [27]).

There are also some researchers trying to combine the adaptive strategy with stabilization method, such as [9,28]. In this paper, we try to combine VMS with *h*-adaptive technique, and the combination is particularly efficient and combines the best algorithmic features of each. Although, a posteriori error estimator is derived based on a projection operator, but by using two local Gauss integrations, this estimator can be computed easily at the element level. The global upper bound for the error of the finite element discretization is yielded follows some assumptions.

☆ Supported by NSF of China (Grant Nos. 10871156 and 10971165) and XJTU (Grant No. 2009xjtujc30).
* Corresponding author. Tel.: +86 29 82675559; fax: +86 29 83237910.
*E-mail addresses:* hbzheng13@gmail.com (H. Zheng), yrhou@mail.xjtu.edu.cn (Y. Hou), fengshi81@yahoo.com.cn (F. Shi).

0021-9991/$ - see front matter © 2010 Elsevier Inc. All rights reserved.
doi:10.1016/j.jcp.2010.05.038

The outline of the paper is as follows. Section 2 introduces the governing equations, the notations and some well-known results used for variational multiscale methods of the Navier–Stokes problem throughout the paper. The posteriori error estimator based on local projection is presented in Section 3, and the equivalent version based on two local Gauss integrations is derived. In Section 4, some numerical simulations are presented to illustrate the efficiency of the combination of VMS with adaptive strategy. We finish with a short conclusion in Section 5.

## 2. Governing equations

We consider the incompressible flows

$$\begin{aligned} &-\nu\Delta u+(u\cdot\nabla)u+\nabla p=f \quad \text{in} \quad \Omega,\\ &\nabla\cdot u=0 \quad \text{in} \quad \Omega,\\ &u=0 \quad \text{on} \quad \partial\Omega, \end{aligned} \tag{2.1}$$

where $\Omega$ represents a polyhedral domain in $R^d$, $d=2,3$ with boundary $\partial\Omega$, $u$ the velocity vector, $p$ the pressure, $f$ the prescribed body force, and $\nu>0$ the kinematic viscosity, which is inversely proportional to the Reynolds number Re.

The standard variational formulation of (2.1) is given by: find $(u,p)\in(V,S)$ satisfying

$$\mathbf{B}(u,p;v,q)+b(u,u,v)=(f,v)\quad\forall(v,q)\in(V,S), \tag{2.2}$$

where

$$\begin{aligned} &V=H_0^1(\Omega)^d \quad\text{and}\quad S=L_0^2(\Omega)=\left\{q\in L^2(\Omega);\int_\Omega q\,d\mathbf{x}=0\right\},\\ &\mathbf{B}(u,p;v,q)=\nu(\nabla u,\nabla v)-(\nabla\cdot v,p)+(\nabla\cdot u,q),\quad b(u,u,v)=((u\cdot\nabla u),v), \end{aligned}$$

with $(\cdot,\cdot)$ the inner product in $L^2(\Omega)$ or in its vector value versions. The norm and seminorm in $H^k(\Omega)^d$ are denoted by $\|\cdot\|_k$ and $|\cdot|_k$, respectively. $H_0^1(\Omega)$ will denote the closure of $C_0^\infty$ with respect to the norm $\|\cdot\|_1$. The space $V$ is equipped with the norm $\|\nabla\cdot\|_0$ or its equivalent norm $\|\cdot\|_1$ due to the Poincaré inequality.

For the finite element discretization, let $\tau_h$ be the regular triangulations of the domain $\Omega$, and define the mesh parameter $h=\max_{T\in\tau_h}\{\mathrm{diam}(T)\}$. We choose the conforming velocity–pressure finite element space $(V_h,S_h)\subset(V,S)$ satisfying the discrete inf-sup condition

$$\inf_{q_h\in S_h}\sup_{v_h\in V_h}\frac{(q_h,\nabla\cdot v_h)}{\|q_h\|_0\|\nabla v_h\|_0}\geqslant\beta>0, \tag{2.3}$$

where $\beta$ is independent of $h$. Here we consider the Taylor–Hood elements (see [29,30]):

$$\begin{aligned} &V_h=\left\{u_h\in C(\Omega)^d|u_h|_T\in P_2(T)^d,\quad\forall T\in\tau_h\right\},\\ &S_h=\left\{q_h\in C(\Omega)|q_h|_T\in P_1(T),\quad\forall T\in\tau_h\right\}, \end{aligned}$$

where $P_k(T)$, $k=1,2$ is the space of $k$th-order polynomials on $T$. We will also need the piecewise constant space

$$R_0=\{v_h\in L^2(\Omega)|v_h|_T\in P_0(T),\quad\forall T\in\tau_h\},$$

where $P_0(T)$ is the space of all constant polynomials on $T$.

Throughout this paper, we shall use the letter $C$ (with or without subscripts) to denote a generic positive constant which may stand for different values at its different occurrences but that remains independent of the mesh parameter $h$.

Then, Galerkin finite element discretization of (2.2) is given by: find $(u_h,p_h)\in(V_h,S_h)$ satisfying

$$\mathbf{B}(u_h,p_h;v_h,q_h)+b(u_h,u_h,v_h)=(f,v_h)\quad\forall(v_h,q_h)\in(V_h,S_h). \tag{2.4}$$

Because of inequality (2.3), problem (2.4) has a unique solution and the error estimate

$$\|\nabla(u-u_h)\|_0+\|p-p_h\|_0\leqslant Ch^2\{\|u\|_3+\|p\|_2\}, \tag{2.5}$$

holds provided $(u,p)\in(H^3(\Omega)^d,H^2(\Omega))$.

As we know, the Galerkin finite element discretization (2.4) is unstable in the case of higher Reynolds number (or smaller viscosity). Therefore, stabilization becomes necessary. We firstly consider a common version of VMS methods which was proposed in [21] for the steady case. We define two spaces $L=L^2(\Omega)^{d\times d}$ and $L_h=R_0(\Omega)^{d\times d}$, the latter is defined on the same grid as $X_h$ for the velocity deformation tensor. The VMS we consider here is: find $(u_h,p_h)\in(V_h,S_h)$ and $g_h\in L_h$ satisfying

$$\begin{aligned} &(\nu+\alpha)a(u_h,v_h)-\alpha(g_h,\nabla v_h)+b(u_h,u_h,v_h)-d(p_h,v_h)=(f,v_h)\quad\forall v_h\in V_h,\\ &d(q_h,u_h)=0\quad\forall q_h\in S_h,\\ &(g_h-\nabla u_h,l_h)=0\quad\forall l_h\in L_h. \end{aligned} \tag{2.6}$$

Here, $a(u,v)=(\nabla u,\nabla v)$ and $d(p,v)=(\nabla\cdot v,p)$. This system is determined by the choices of $L_h$ and $\alpha$. The stabilization parameter $\alpha$ in this scheme acts only on the small scales.

It is easy to verify that the last equation in (2.6) implies that $g_h$ is the $L^2$ projection of $\nabla u_h$ onto $L_h$. Now we define the orthogonal projection operator $\Pi_v$: $L\to L_h$ with the following properties:

$$((I-\Pi_v)l,g_h)=0\quad \forall l\in L,\quad g_h\in L_h, \tag{H1}$$
$$\|\Pi_v l\|_0\leqslant C\|l\|_0\quad \forall l\in L, \tag{H2}$$
$$\|(I-\Pi_v)l\|_0\leqslant Ch\|l\|_1\quad \forall l\in L\cap H^1(\Omega)^{d\times d}. \tag{H3}$$

Here, $I$ is the identity operator.

Then (2.6) can be rewritten as

$$\begin{aligned} &va(u_h,v_h)+\alpha((I-\Pi_v)\nabla u_h,\quad (I-\Pi_v)\nabla v_h)+b(u_h,u_h,v_h)-d(p_h,v_h)=(f,v_h)\quad \forall v_h\in V_h,\\ &d(q_h,u_h)=0\quad \forall q_h\in S_h. \end{aligned} \tag{2.7}$$

Assume that there are local singularities of the solution of the continuous problem, or, in the critical regions the solution is less regular, such that the error estimate

$$\|\nabla(u-u_h)\|_0+\|p-p_h\|_0\leqslant Ch\{\|u\|_2+\|p\|_1\} \tag{2.8}$$

holds provided $(u,p)\in(H^2(\Omega)^d,H^1(\Omega))$, so that, the accuracy of the numerical solution is degraded.

**Remark 1.** To our knowledge, for higher Reynolds number, the constant $\alpha$ should be chosen as the scale of $O(h)$ in order to stabilize the convective term appropriately. For simplicity, all later experiments are taken with $\alpha=0.1$ h.

**Remark 2.** As discussed in [27], (2.7) has an equivalent version based on two local Gauss integrations: find $(u_h,p_h)\in(V_h,S_h)$ such that

$$\begin{aligned} &va(u_h,v_h)+G(u_h,v_h)+b(u_h,u_h,v_h)-d(p_h,v_h)=(f,v_h)\quad \forall v_h\in X_h,\\ &d(q_h,u_h)=0\quad \forall q_h\in S_h. \end{aligned} \tag{2.9}$$

Here,

$$G(u_h,v_h)=\alpha\sum_{T\in\tau_h}\left\{\int_{T,k}\nabla u_h\nabla v_h d\mathbf{x}-\int_{T,1}\nabla u_h\nabla v_h d\mathbf{x}\right\}\quad \forall u_h,v_h\in V_h,$$

where $\int_{T,i}g(x)d\mathbf{x}$ indicates an appropriate Gauss integral over $T$ that is exact for polynomials degree $i$, $i=1$, $k(k\geqslant 2)$.

In numerical experiments, we will use (2.9) to represent (2.6) for all cases, because the equivalence between them, it will not affect our results, but save computational times.

Additionally, under some mild assumptions on $\tau_h$, the following inverse inequality holds [31] which will be used later:

$$\|\nabla q_h\|_0\leqslant C_I h^{-1}\|q_h\|_0\quad q_h\in R_1. \tag{2.10}$$

Spaces consisting of vector-valued functions will hold too.

## 3. A projection error estimator based on two local Gauss integrations

Before deriving the projection estimator, we define operator $\Pi_p$: $L^2(\Omega)\to R_0$ acting on the pressure. Obviously, $\Pi_p$ has the same properties as $\Pi_v$, but has the form of scalar value. Later we will not distinguish $\Pi_v$ and $\Pi_p$, both denoted by $\Pi$, for simplicity.

Then, our global projection estimator is based on the residual between the gradient of the velocity $\nabla u_h$, the pressure $p_h$ and their projection $\Pi\nabla u_h$ and $\Pi p_h$. More precisely, we define as follows

$$\eta_{\Pi,T}:=\|(I-\Pi)\nabla u_h\|_{0,T}+\|(I-\Pi)p_h\|_{0,T}.$$

Then, based on orthogonal projection properties of operator $\Pi$ and two local Gauss integrations technique presented in [27,32], our local projection error estimator will be presented more precisely and computationally based on two local Gauss integrations as follows:

$$\begin{aligned} \eta(u_h,p_h)_{\Pi,T}&:=\|(I-\Pi)\nabla u_h\|_{0,T}+\|(I-\Pi)p_h\|_{0,T}\cong\left\{\|(I-\Pi)\nabla u_h\|_{0,T}^2+\|(I-\Pi)p_h\|_{0,T}^2\right\}^{1/2}\\ &\cong\left\{\|\nabla u_h\|_{0,T}^2-\|\Pi\nabla u_h\|_{0,T}^2+\|p_h\|_{0,T}^2-\|\Pi p_h\|_{0,T}^2\right\}^{1/2}\cong\left\{\int_{T,k}(\nabla u_h)^2+(p_h)^2d\mathbf{x}-\int_{T,1}(\nabla u_h)^2+(p_h)^2d\mathbf{x}\right\}^{1/2}. \end{aligned}$$

For all 1th-order polynomials, $\nabla u_h(T)$ and $p_h(T)$ must be piecewise constants when $i=1$. Then, the globally error estimator is defined by:

$$\eta_{\Pi} = \left\{ \sum_{T\in\tau_h} \eta_{\Pi,T}^2 \right\}^{1/2}.$$

**Remark 3.** Here $\cong$ denotes the equivalence. The equivalence just follows

$$\|\Pi w\|_{0,T}^2 = \int_{T,1} w^2 d\mathbf{x}.$$

Here $w$ can be $\nabla u_h$ or $p_h$.

We just discuss the case $w = p_h$, for simplicity, the proof is the same for deformation tensor $w = \nabla u_h$.

Assume that $q_i$, $i = 1,2,3$ are the three vertices of an element $T$. For $p_h \in S_h$, we obtain

$$\int_{T,1} (p_h)^2 d\mathbf{x} = \int_{T,k} \left[ p_h\left(\frac{q_1+q_2+q_3}{3}\right)\right]^2 d\mathbf{x} = \int_{T,k} \left[\frac{p_h(q_1)+p_h(q_2)+p_h(q_3)}{3}\right]^2 d\mathbf{x} = \int_{T,k} (\Pi p_h)^2 d\mathbf{x} = \|\Pi p_h\|_{0,T}^2.$$

The equivalence is true.

**Remark 4.** Based on two local Gauss integrations, $\eta(u_h,p_h)_{\Pi,T}$ can be computed explicitly. Before giving the global upper bound, we recall a lemma in [33] will be useful later.

**Lemma 3.1.** *There exists a positive constant C such that*

$$Ch\|\nabla p_h\|_0 \leqslant \|(I-\Pi)p_h\|_0 \quad \forall p_h \in S_h. \tag{3.1}$$

**Proof.** To make the context complete, we also give the proof. From the definition of spaces $S_h$, we note that $p_h$ is continuous and $\Pi p_h$ is constant on each element $T$, such that $\nabla(\Pi p_h)|_T = 0$. As a result, using the inverse inequality (2.10),

$$h^2\|\nabla p_h\|_0^2 = \sum_{T\in\tau_h} h^2\|\nabla p_h\|_{0,T}^2 = \sum_{T\in\tau_h} h^2\|\nabla(I-\Pi)p_h\|_{0,T}^2 \leqslant \sum_{T\in\tau_h} C_I^2\|(I-\Pi)p_h\|_{0,T}^2 = C\|(I-\Pi)p_h\|_0^2.$$

Then, the lemma is proved. □

For $\nabla u_h \in R_1^{d\times d}$, spaces consisting of vector-valued functions will also hold:

$$Ch\|\nabla u_h\|_1 \leqslant \|(I-\Pi)\nabla u_h\|_0 \quad \forall u_h \in V_h. \tag{3.2}$$

**Theorem 3.2.** *There is a constant C, which only depend on the smallest angle in the triangulation $\tau_h$ and the domain $\Omega$, such that, we have the following global upper bounds:*

$$\|\nabla(u-u_h)\|_0 + \|p-p_h\|_0 \leqslant C\eta_{\Pi}, \tag{3.3}$$

*where C independent of h.*

**Proof.** Because of the stability of (2.2) and (2.7), then, we assume that, there are two positive constants $C_l$, $C_u$ such that:

$$C_l \leqslant \|p\|_1, \quad \|p_h\|_1, \quad \|u_h\|_2, \quad \|u\|_2 \leqslant C_u.$$

Following the discuss of Lemma 3.1, and using the triangle inequality, we yield

$$\|\nabla(u-u_h)\|_0 + \|p-p_h\|_0 \leqslant Ch\|u\|_2 + Ch\|p\|_1 \leqslant C\frac{C_u}{C_l}h\|\nabla u_h\|_1 + C\frac{C_u}{C_l}h\|p_h\|_1 \leqslant C\{\|(I-\Pi)\nabla u_h\|_0 + \|(I-\Pi)p_h\|_0\} \leqslant C\eta_{\Pi}.$$

This is (3.3). □

## 4. Numerical tests

In this section we report several experiments to verify the stability and accuracy of the combination of VMS with adaptive technique. The numerical examples are broadly divided into two parts. The first part presents a singular problem. The second part deals with the problem of nonlinear steady flow with high Reynolds numbers.

### 4.1. Implementation

In all experiments, the algorithms are implemented using public domain finite element software [34].

For completeness, we give the main idea of the refinement strategy presented in [34] for the algorithm of the discrete problem (2.9). Starting from the original triangulation $\tau_0$ of a polygonal approximation $\Omega$, we construct a sequence of refined

triangulations $\tau_j$ as follows. Given $\tau_j$, first, we compute the solution $(u_j, p_j)$ from the problem (2.9), then, we compute the error estimator $\eta^j_{\Pi,T}$, the new mesh size is given by the following formulae:

$$h_{j+1} = \frac{h_j}{f_j\left(\eta^j_{\Pi,T}\right)},$$

where $h_j$ is the previous "meshsize" field, and $f_j$ is a user function defined by

$$f_j = \min\left(\max\left(\eta^j_{\Pi,T}/(c\overline{\eta^j}), 1.0000\right), 3\right),$$

where $\overline{\eta^j}$ means the mean of $\eta^j_{\Pi,T}$, $c$ is an user coefficient generally close to one and the numbers 1.0000, 3 also can be changed by the user according to the requirement.

For simplicity, in all latter tests, $c = 0.8$ will be our choice. Certainly, we also can consider other refinement strategy, such as in [4], there will not be much differences between them.

The computation adaptive strategy here is made of two steps.

First, choose a tolerance $\eta^s$, start from the original triangulation $\tau_0$, compute the $\eta_\Pi$.

- Step 1: If $\eta_\Pi \leqslant \eta^s$, stop, and we obtain the final finite element solution. Otherwise, we go to Step 2.
- Step 2: Compute the $\eta_{\Pi,T}$ and their mean value $\bar{\eta}$, and generate a new mesh size $h$ by the above strategy, then solve the discrete problem (2.9) and recompute $\eta_\Pi$ based on this new triangulation. Go back to Step 1.

### 4.2. A singular problem

First, we consider $\Omega$ as a disk of radius 1 with a crack joining the center to the boundary as presented in [4] and the exact solution the velocity $u = (u_1, u_2)$ and pressure $p$ is given as follows:

$$u_1 = 1.5r^{1/2}(\cos(0.5\theta) - \cos(1.5\theta)),$$
$$u_2 = 1.5r^{1/2}(3\sin(0.5\theta) - \sin(1.5\theta)),$$
$$p = -6/r^{1/2}\cos(0.5\theta),$$

where $(r, \theta)$ is a polar representation of a point in the disk and is singular at the end of the crack, i.e., at the center of the disk. With low Reynolds number Re = 1, $f$ is determined by (2.1) and $u$ is enforced with appropriate inhomogeneous boundary conditions.

For convenience of presentation, we introduce the following notations:

- $|||(e_h, \varepsilon_h)||| =: \|\nabla(u - u_h)\|_0 + \|p - p_h\|_0$;
- $e_r =:$ the relative error of $|||(e_h, \varepsilon_h)|||$;
- $\mathrm{DOF}_j :=$ number of elements in $\tau_j$;
- ratio $:= \frac{2*\log(e_j/e_{j-1})}{\log(\mathrm{DOF}_{j-1}/\mathrm{DOF}_j)}$, experimental order of convergence of $e_j$, $e_j$ can be the related true error or the projection estimator;
- $E := \eta^j_\Pi / |||(e^j_h, \varepsilon^j_h)|||$, effective index, i.e., the ratio between the projection estimator and the true error.

The uniform and adaptive refinements both begin with the same initial meshes as shown in left part of Fig. 4.1. Also the final uniform and adaptive refinement are presented in middle and right part of this figure, respectively. Pressure level lines are plotted on related grids (see Fig. 4.2). In Tables 4.1 and 4.2 we list the convergence analysis and effectivity ratio for both uniform and adaptive cases.

The observations and conclusions of this experiment are presented as follows:

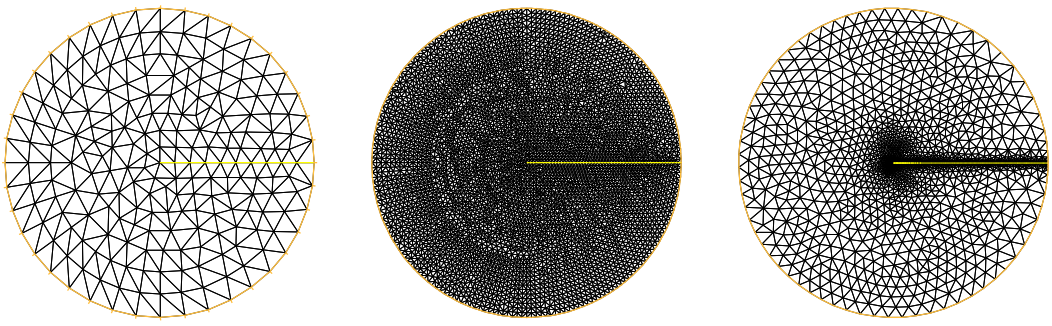

**Fig. 4.1.** From left to right: initial meshes; final refinement at uniform case; final refinement at adaptive case.

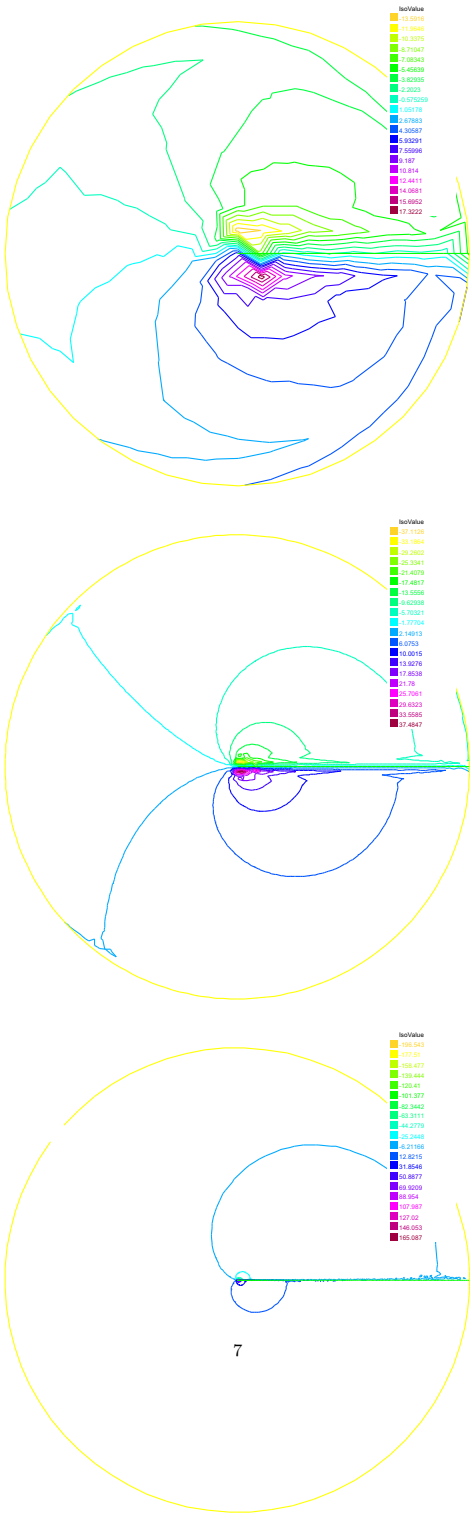


**Fig. 4.2.** The pressure line on related triangulations. Form the top down: initial meshes; final refinement at uniform case; final refinement at adaptive case.

- From Fig. 4.1, we notice that the adaptive strategy creates a lot of triangles in the area near the end of the crack, where the singularity arises, but uniform case refines everywhere.
- After some successive iterations, for both case, compared with the initial pressure, the pressure based on final uniform and adaptive refinement will be less singularity and more smooth. Although, in this figure, the result in the uniform case

**Table 4.1**
Convergence analysis and effectivity ratio for a sequence of uniform meshes.

| Level | DOF | CPU | $e_r$ | $\eta_\Pi$ | $E$ |
|---|---|---|---|---|---|
| 1 | 396 | 3.30 | 0.4034 | 2.1866 | 0.4011 |
| 2 | 1588 | 13.27 | 0.3076 | 1.7057 | 0.4095 |
| 3 | 3604 | 29.30 | 0.2614 | 1.4925 | 0.4222 |
| 4 | 6404 | 57.78 | 0.2276 | 1.3469 | 0.4374 |
| 5 | 9980 | 93.17 | 0.2076 | 1.2153 | 0.4322 |
| Ratio | – | – | 0.4116 | 0.3640 | – |

**Table 4.2**
Convergence analysis and effectivity ratio for a sequence of adapted meshes.

| Level | DOF | CPU | $e_r$ | $\eta_\Pi$ | $E$ |
|---|---|---|---|---|---|
| 1 | 396 | 2.47 | 0.4034 | 2.1866 | 0.4011 |
| 2 | 800 | 7.61 | 0.2513 | 1.5927 | 0.4685 |
| 3 | 1437 | 16.99 | 0.1547 | 1.1668 | 0.5575 |
| 4 | 2726 | 35.02 | 0.1005 | 0.8409 | 0.6181 |
| 5 | 5128 | 66.82 | 0.0669 | 0.6037 | 0.6662 |
| Ratio | – | – | 1.4032 | 1.0051 | – |

still gets small oscillation, while in adaptive grids, the pressure is very smooth. When the mesh is fine enough, the uniform case will also obtain a smooth solution, however, it will require much more degrees of freedom than the adaptive case.

- As shown in Tables 4.1 and 4.2, according to the relative error $e_r$, uniform refinements do not derive good approximation, even using much more meshes, we still cannot get a better result, actually, the ratio is only near to 0.4, too poor to use uniform strategy to approximate the true solution, which will ask for more storage memory and CPU time. On the other hand, the adaptive strategy obtains much better approximation solution, and the ratio arises to nearly 1.4, although this still does not reach to the optimal convergence order, but it requires less meshes and gets much better accuracy, and will be very significant in practice, especially, in 3D case. The corresponding CPU time for the runs with errors are also shown in Tables 4.1 and 4.2, we can see that the adaptive strategy will save much CPU time than the uniform strategy. Additionally, in uniform case, the effectivity $E$ only approaches 0.4, while in adaptive case, $E$ increases from 0.40 to 0.66 successively level by level, which is better than the uniform case.

### 4.3. Lid driven cavity

Our second examples is the 'lid driven cavity' which is a popular benchmark problem for testing numerical schemes. In this test, fluid is enclosed in a square box, with an imposed velocity of unity in the horizontal direction on the top boundary, and a no slip condition on the remaining walls. The computational results of VMS based on uniform and adaptive refinements for a set of different higher Reynolds numbers (Re = 3200, 5000, 10,000) are shown in the Figs. 4.3–4.9 and 4.10 and Table 4.3, compared with the results obtained by Ghia et al. [35].

In uniform (but unstructured) case, the successive meshes are obtained with the Delaunay triangulation at $h = 1.0/N$. We will choose $N = 32, 48, 64$ according to the related Reynolds number, and $\alpha = 0.1$ h will be chosen for all cases. In adaptive

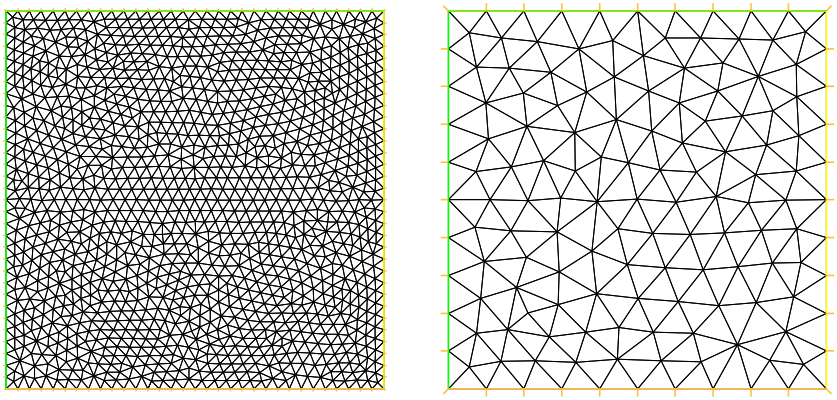

**Fig. 4.3.** Triangulations for uniform and adaptive cases. Left: uniform case (but unstructured), $N = 32$; Right: initial triangulation for adaptive case with different Reynolds numbers.

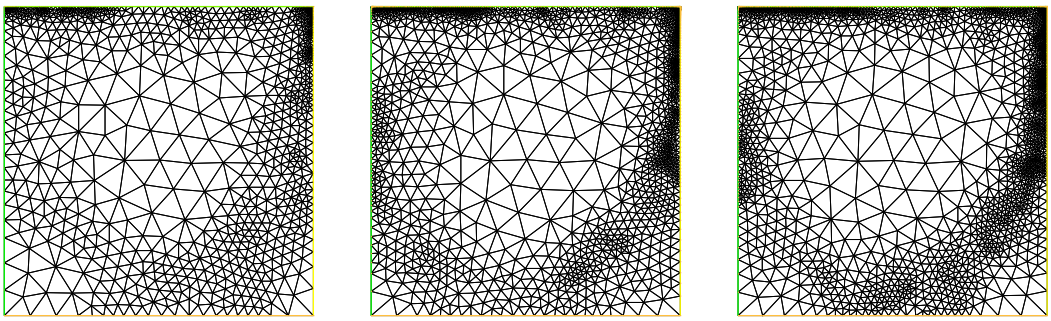

**Fig. 4.4.** Final adaptive refinements for the driven cavity with related Reynolds numbers. From left to right: Re = 3200, 5000, 10,000.

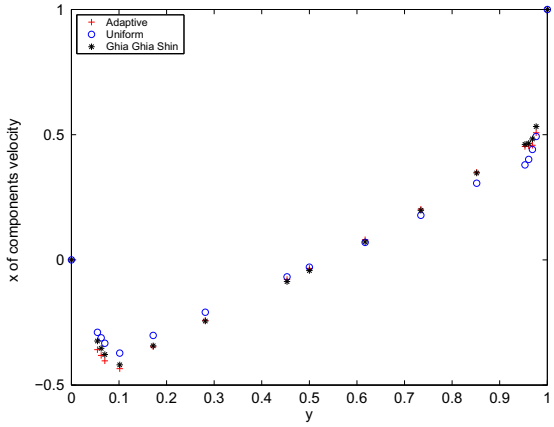


**Fig. 4.5.** Vertical midlines for Re = 3200.

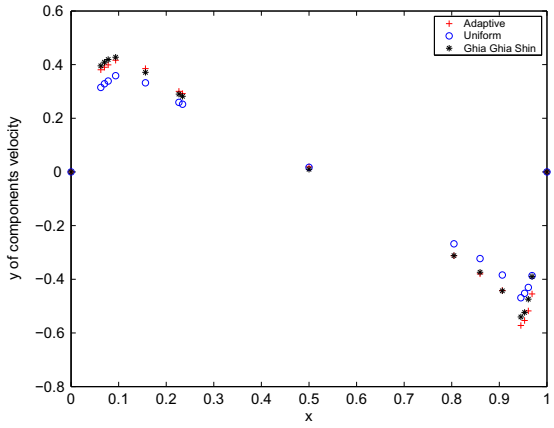


**Fig. 4.6.** Horizontal midlines for Re = 3200.

strategy, we start with an initial mesh generated with the Delaunay triangulation at $h = 0.1$. The parameters for adaptive case also will be taken as done in uniform case. The mesh for $N = 32$ is shown in left part of Fig. 4.3, the right part of this figure is the commonly used initial triangulation for adaptive refinements for all Reynolds numbers.

Grids on final adaptive refinements for different Reynolds numbers are plotted in Fig. 4.4. For all triangulations, we observe that the region around the primary vortex are hardly refined, but a lot of triangles create in the two upper corners of the cavity due to the singularities. Because of the discontinuities in the boundary conditions, the upper and the right boundary also require much refinements. Besides, in the right bottom corner of the cavity where the second vortex

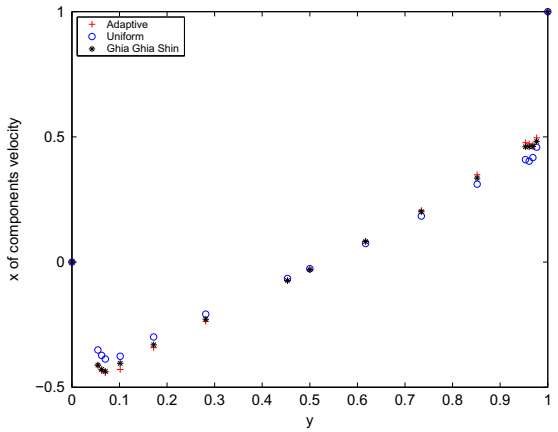


**Fig. 4.7.** Vertical midlines for Re = 5000.

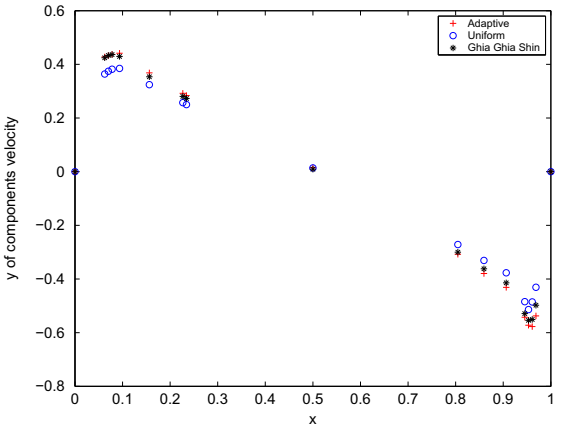


**Fig. 4.8.** Horizontal midlines for Re = 5000.

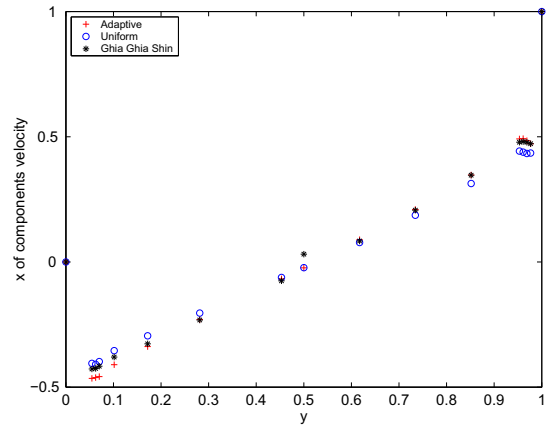


**Fig. 4.9.** Vertical midlines for Re = 10,000.

may appear and at the lower left corner in which a third vortex appears, adaptive strategy also will not take more refinements.

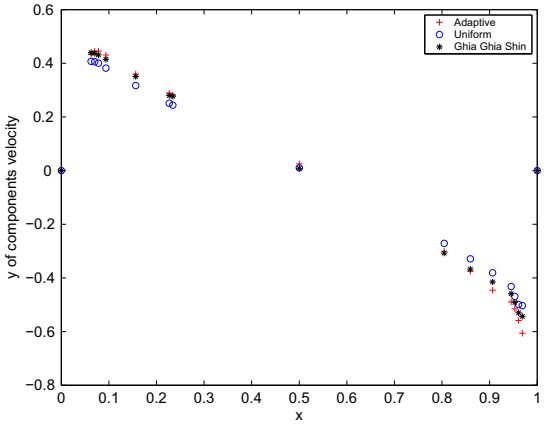


**Fig. 4.10.** Horizontal midlines for Re = 10,000.

**Table 4.3**
Meshes and CPU time for VMS on uniform refinement and final adaptive refinement, respectively.

| Strategy | Re | 3200 | 5000 | 10,000 |
|---|---|---|---|---|
| Uniform | DOF | 2430 | 5474 | 9694 |
| | CPU | 492.58 | 1274.28 | 3526.06 |
| Adaptive | DOF | 1913 | 3611 | 4402 |
| | CPU | 407.91 | 886.28 | 1710.98 |

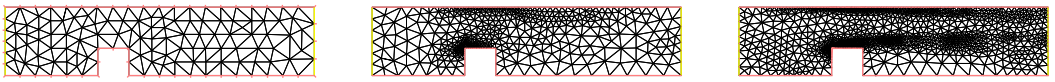

**Fig. 4.11.** Triangulations for the step problem with Re = 1000. From left to right: initial meshes $\tau_0$; second refinement $\tau_2$; final refinement $\tau_4$.

In particular, we draw the $x$ component of velocity along the vertical centerline and $y$ component of velocity along the horizontal centerline. Ghia et al.'s algorithm is based on the time dependent stream function using the coupled implicit and multigrid methods (see Figs. 5.2–5.9). Compared with the fairly finer mesh ($h = 1/129$, DOF $\approx 34{,}000$) in [35], the uniform numerical simulations are computed on a mesh (DOF = 2430,5474,9694) and the final adaptive case requires meshes (DOF = 1913,3611,4402). Good agreement with the benchmark data of Ghia et al. [35] verify both cases. Moreover, the combination of VMS with adaptive strategy approaches the benchmark data much better than the uniform case somewhere.

To show the effectiveness of VMS based on adaptive strategy than VMS based on uniform strategy, we give the CPU time in Table 4.3 following the above tests. From this table, we can see that adaptive case will need less meshes and save more CPU time as Re increases than uniform case.

### *4.4. Navier–Stokes flow over a step*

Finally, we consider the Navier–Stokes flow over a step with high Reynolds number Re = 1000. The computational domain is given by $\Omega = (0,4) \times (0,1)/(1.2,1.6) \times (0,0.4)$, and the flow is enforced with Dirichelet condition $u = (0,0)$ at upper and lower computational boundaries, natural boundary condition at the outflow while $u = (4{*}y{*}(1-y),0)$ at the inflow. Here the spikes in the pressure are due to a discontinuity in the geometry of the boundary. Figs. 4.11 and 4.12 show that the different adaptive refinements and the related contour plots of the pressure based on these grids, respectively. In this example, a singularity arises at the step from the re-entrant corner. Fig. 4.11 shows that there are more grids added near the upper corner of the step after some successive iterations. From Fig. 4.12, we know that initial grid introduces numerical dissipation, while after enough adaptive iterations, the profile of pressure gets better representation with less dissipation.

## 5. Conclusions

In this paper, we have designed and analyzed a posteriori error estimate for variational multiscale methods of the steady Navier–Stokes problem based on a projection estimator. The discussions and the numerical tests showed that the projection

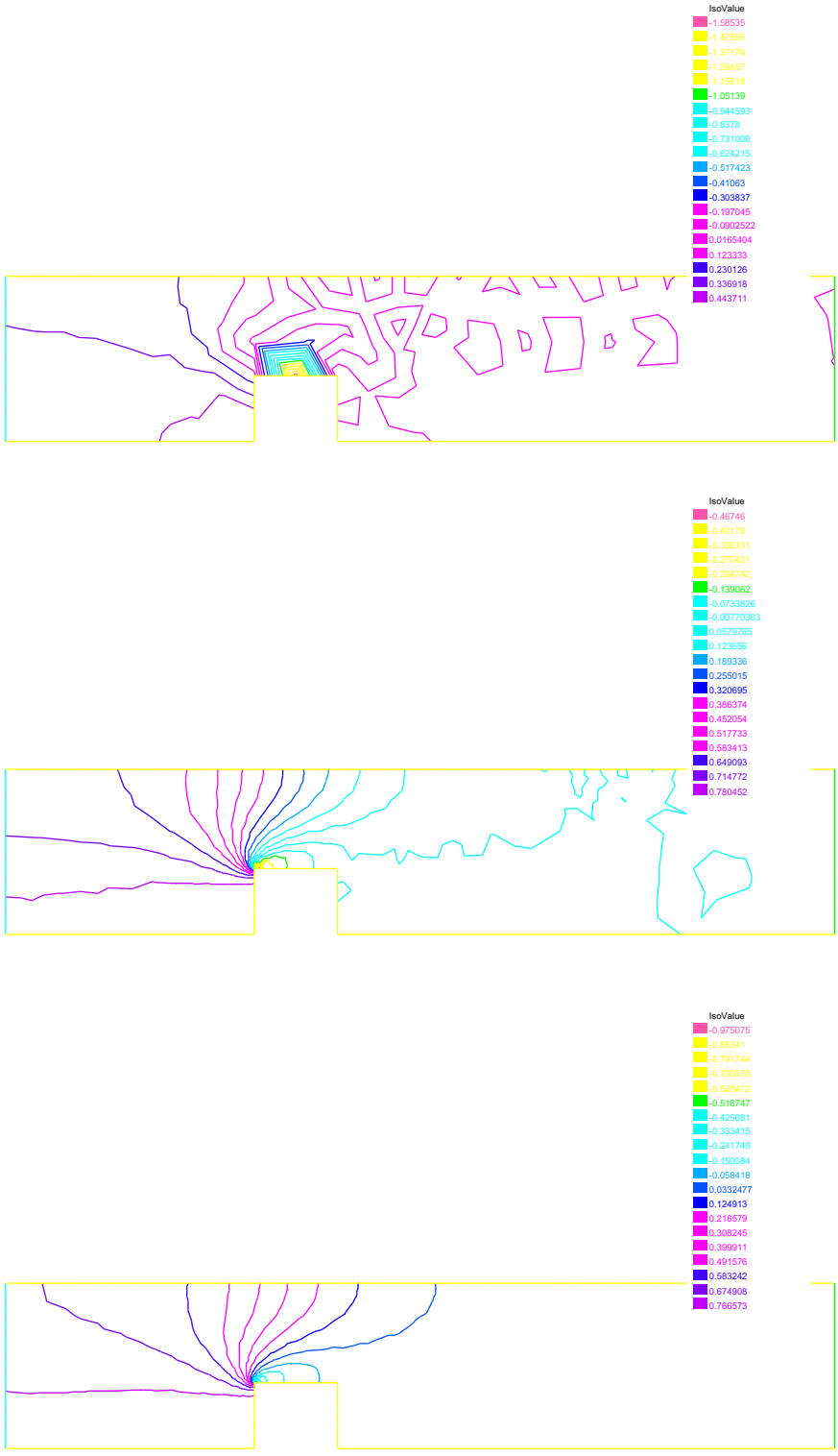


**Fig. 4.12.** The related pressure level lines on different grids. From the top down: initial meshes $\tau_0$; second refinement $\tau_2$; final refinement $\tau_4$.

estimator is computational and efficiency. This combination of VMS and adaptive technique has strong promise, but many open questions remain including the correct extension of the method to time dependent problems, further analysis of the local upper and lower bounds, and so on.

## References


[1] I. Babuska, W.C. Rheinboldt, A posteriori error estimates for the finite element method, Int. J. Numer. Methods Eng. 12 (1978) 1597–1615.
[2] I. Babuska, W.C. Rheinboldt, Error estimates for adaptive finite element computations, SIAM J. Numer. Anal. 15 (1978) 736–754.
[3] R.E. Bank, A. Weiser, Some a posteriori error estimators for elliptic partial differential equations, Math. Comp. 44 (1985) 283–301.
[4] R. Verfurth, A posteriori error estimators for the Stokes equations, Numer. Math. 55 (1989) 309–325.
[5] R. Verfurth, A Review of a Posteriori Error Estimation and Adaptive Mesh-Refinement Techniques, Wiley/Teubner, Stuttgart, 1996.
[6] R.E. Bank, B.D. Welfert, A posteriori error estimates for the Stokes problem, SIAM J. Numer. Anal. 28 (1991) 591–623.
[7] M. Ainsworth, J.T. Oden, A posteriori error estimators for the Stokes and Oseen equations, SIAM J. Numer. Anal. 34 (1997) 228–245.
[8] H.B. Zheng, Y.R. Hou, F. Shi, A posteriori error estimates of stabilization of low-order mixed finite elements for incompressible flow, SIAM J. Sci. Comput. 32 (2010) 1346–1360.
[9] V.J. Ervin, W.J. Layton, J.M. Mauvach, Adaptive defect-correction methods for viscous incompressible flow problems, SIAM J. Numer. Anal. 37 (2000) 1165–1185.
[10] O.C. Zienkiewicz, J. Zhu, A simple error estimator and adaptive procedure for practical engineering analysis, Int. J. Numer. Methods Eng. 24 (1987) 337–357.
[11] O.C. Zienkiewicz, J. Zhu, The superconvergence patch recovery and a posteriori error estimates, Part I: the recovery technique, Int. J. Numer. Methods Eng. 33 (1992) 1331–1364.
[12] O.C. Zienkiewicz, J. Zhu, The superconvergence patch recovery and a posteriori error estimates, Part II: error estimates and adaptivity, Int. J. Numer. Methods Eng. 33 (1992) 1365–1382.
[13] R.E. Bank, J. Xu, Asymptotically exact a posteriori error estimators, Part I: grids with superconvergence, SIAM J. Numer. Anal. 41 (2003) 2294–2312.
[14] J. Xu, Z. Zhang, Analysis of recovery type a posteriori error estimators for mildly structured grids, Math. Comp. 73 (2004) 1139–1152.
[15] A. Naga, Z. Zhang, A posteriori error estimates based on the polynomial preserving recovery, SIAM J. Numer. Anal. 42 (2004) 1780–1800.
[16] Z. Zhang, A. Naga, A new finite element gradient recovery method: superconvergence property, SIAM J. Sci. Comput. 26 (2005) 1192–1213.
[17] J.-L. Guermond, Stabilization of Galerkin approximations of transport equations by subgrid modeling, M2AN Math. Model. Numer. Anal. 33 (1999) 1293–1316.
[18] T.J.R. Hughes, L. Mazzei, A.A. Oberai, The multiscale formulation of large eddy simulation: decay of homogeneous isotropic turbulence, Phys. Fluids 13 (2001) 505–511.
[19] T. Hughes, L. Mazzei, K. Jansen, Large eddy simulation and the variational multiscale method, Comput. Vis. Sci. 3 (2000) 47–59.
[20] T.J.R. Hughes, Multiscale phenomena: Green's functions the Dirichlet-to-Neumann formulation subgrid-scale models bubbles and the origins of stabilized methods, Comput. Methods Appl. Mech. Eng. 127 (1995) 387–401.
[21] W. Layton, A connection between subgrid-scale eddy viscosity and mixed methods, Appl. Math. Comput. 133 (2002) 147–157.
[22] S. Kaya, B. Riviere, A twogrid stabilization method for solving the steadystate Navier–Stokes equations, Numer. Methods PDEs. 3 (2006) 728–743.
[23] S. Kaya, W. layton, B. Riviere, Subgrid stabilized defect-correction methods for the Navier–Stokes equations, SIAM. Numer. Anal. 44 (2006) 1639–1654.
[24] V. John, S. Kaya, Finite Element Error Analysis of a Variational Multiscale Method for the Navier–Stokes Equations, Otto-von-Guericke Universitat Magdeburg, Fakultat fur Mathematik, 2004, preprint.
[25] V. John, S. Kaya, A finite element variational multiscale method for the Navier–Stokes equations, SIAM J. Sci. Comput. 26 (2005) 1485–1503.
[26] V. John, S. Kaya, W. Layton, A two-level variational multiscale method for convection-dominated convection-diffusion equations, Comput. Methods Appl. Mech. Eng. 195 (2006) 4594–4603.
[27] H.B. Zheng, Y.R. Hou, F. Shi, L.N. Song, A finite element variational multiscale method for incompressible flows based on two local Gauss integrations, J. Comput. Phys. 228 (2009) 5961–5977.
[28] S. Berrone, Adaptive discretization of stationary and incompressible Navier–Stokes equations by stabilized finite element methods, Comput. Methods Appl. Mech. Eng. 190 (2001) 4435–4455.
[29] V. Girault, P.-A. Raviart, Finite Element Methods for the Navier–Stokes Equations: Theory and Algorithms, Springer Series in Computer Mathematics, vol. 5, Springer, Berlin, 1986.
[30] M. Gunzburger, Finite Element Methods for Viscous Incompressible Flows: A Guide to Theory, Practice and Algorithms, Academic Press, Boston, 1989.
[31] P.G. Ciarlet, The Finite Element Method for Elliptic Problems, vol. 40, SIAM Classics in Appl. Math., SIAM, Philadelphia, 2002.
[32] J. Li, Y.N. He, A stabilized finite element method based on two local Gauss integrations for the Stokes equations, J. Comp. Appl. Math. 214 (2008) 58–65.
[33] P.B. Bochev, C.R. Dohrmann, M.D. Gunzburger, Stabilization of low-order mixed finite elements for the Stokes equations, SIAM J. Numer. Anal. 44 (2006) 82–101.
[34] FreeFem++, version 2.17.1. Available from: <http://www.freefem.org/>.
[35] U. Ghia, K.N. Ghia, C.T. Shin, High-resolutions for incompressible flow using the Navier–Stokes equations and a multigrid method, J. Comput. Phys. 48 (1982) 387–411.